Enhanced CO_2 electroreduction with metal-nitrogen-doped carbons in a continuous flow reactor

Enhanced CO_2 electroreduction with metal-nitrogen-doped carbons in a continuous flow reactor

Miguel Duarte ‡ [a], Nick Daems ‡ [ab], Jonas Hereijgers [a], Daniel Arenas-Esteban [c], Sara Bals [c], Tom Breugelmans [ab]*

[a] *Applied Electrochemistry & Catalysis (ELCAT), University of Antwerp, Universiteitsplein 1, 2610 Wilrijk, Belgium*

[b] *Separation & Conversion Technologies, VITO, Boeretang 200, 2400 Mol, Belgium.*

[c] *Electron Microscopy for Materials Science (EMAT), Department of Physics, University of Antwerp, Groenenborgerlaan 171, 2020 Antwerp, Belgium*

‡ These authors contributed equally

*Corresponding author: e-mail Tom.Breugelmans@uantwerpen.be

KEYWORDS

Metal-nitrogen-doped carbons – Electrochemical reduction of CO_2 – Power to chemicals – Flow cell electrolyzers - Electrocatalysis

Abstract

As part of a mitigation and adaptation approach to increasing carbon dioxide atmospheric concentrations, we report superior performance of various metal-nitrogen-doped carbon catalysts, synthesized using an easily up-scalable method, for the electrochemical reduction to carbon monoxide and/or formate at industrially relevant current densities up to 200 $mAcm^{-2}$. Altering the embedded transition metal (i.e. Sn, Co, Fe, Mn and Ni) allowed to tune the selectivity towards the desired product. Mn-N-C and Fe-N-C performance was compromised by its high CO* binding energy, while Co-N-C catalyzed preferentially the HER. Ni-N-C and Sn-N-C revealed to be promising electrocatalysts, the latter being evaluated for the first time in a flow reactor. A productivity of 589 L CO $m^{-2}h^{-1}$ at -1.39 V_{RHE} with Ni-N-C and 751 g $HCOO^{-}$ $m^{-2}h^{-1}$ at -1.47 V_{RHE} with Sn-N-C was achieved with no signs of degradation detected after 24 hours of operation at industrially relevant current densities (100 $mAcm^{-2}$). Stable operation at 200 $mAcm^{-2}$ led to turnover frequencies for the production of carbon products of up to 5176 h^{-1}. These enhanced productivities, in combination with high stability, constitute an essential step towards the scalability and ultimately towards the economical valorization of CO_2 electrolyzers using metal-containing nitrogen-doped catalysts.

1. Introduction

Due to rising concentrations of carbon dioxide (CO_2) in the atmosphere, the Earth's climate is changing at a rate never experienced in human history. The capture and repurposing of carbon dioxide from the atmosphere as a mitigation and adaptation approach is gathering increasing interest from the scientific community. One possible strategy is the electrochemical reduction of CO_2 (ERC) towards the production of various liquid or gaseous products (e.g. carbon monoxide, formic acid, methane, ethylene or methanol) with the use of renewable electricity sources. The production of chemicals from CO_2 is projected to be accountable for the utilization of 300 to 600 Mt CO_2 by 2050 [1]. Carbon monoxide (CO) and formate ($HCOO^-$) are especially interesting products in terms of revenue per mole of electrons, as they only require two electrons per molecule of product. Multiple techno economic assessments, based on current reactor performance and market price, identify these two products as the most promising, most advanced to substitute current petrochemical supply chains [2–4]. CO production is currently largely reliant on the steam reforming of natural gas and other hydrocarbons, which requires high pressure and temperature. Furthermore, it has widespread application in the Fischer Tropsch synthesis [5], fermentation processes [6] or even as an intermediate in the electrochemical production of C_2 and C_3 products [7]. On its turn, formic acid is used as preservative and antibacterial agent and it stands out as ERC product due to its potential use as energy carrier in direct formic acid fuel cells [8].

However, CO_2 is thermodynamically a highly stable molecule requiring high overpotentials, which results in low energy efficiencies. In an attempt to lower this high overpotential, metals have been the preferred choice as electrocatalyst. In most research directed to the ERC towards

CO, state-of-the-art noble metals such as silver [9–11], gold [12,13] or palladium [14] were used, which show a weak binding with the CO* intermediate [15]. Moderate success has been achieved in replacing these precious metal electrodes with earth-abundant materials such as zinc [16], bismuth [17], tungsten diselenide [18] or molybdenum disulphide [19]. Tin is the catalyst of choice for the production of HCOOH [20–22] as well as lead [23,24]. In an attempt to lower the catalyst cost and to improve performance, catalysts based on earth-abundant materials such as doped carbon materials including transition metals (M-N-C) have recently gained scientific attention [25]. M-N-C are traditionally used for the oxygen reduction reaction which has resulted in a profound knowledge of its catalytic behavior [26,27]. The inclusion of heteroatoms such as boron or nitrogen in carbon matrixes breaks the electroneutrality of carbons transforming them into active electrocatalysts [28]. Fundamental catalytic studies have shown that metal-free nitrogen-doped carbons can have its nanostructure tuned for the production of a multitude of ERC products including even C_3 compounds as reported by *Wu et al.* [25], suggesting pyridinic N as leading active site for CO_2 reduction. The latter is in accordance with previous works for the oxygen reduction reaction where pyridinic N is also considered to be (one of) the active sites [29]. The incorporation of nitrogen atoms increases the electron density at the catalyst surface due to its slightly alkaline nature, promoting the adsorption of the slightly acidic CO_2 [30]. Furthermore, pyridinic N has an available lone electron pair for binding with CO_2. Co-doping these frameworks with transition metals allows further controlling its selectivity and further activating the catalyst. Indeed, Pan *et al.* achieved higher current densities with all M-N-C, compared to metal-free nitrogen-doped carbons [28]. *Zhang et al.* furthermore achieved 90% Faradaic efficiency towards CO at 10 mA cm^{-2} with manganese-nitrogen-doped carbons [31]. Very recently, our group analyzed nickel containing nitrogen-doped catalysts and further

combined this analysis with reactor optimization achieving a current density up to 50 mA cm^{-2} at Faradaic efficiencies above 90% towards CO [32]. In another study, Ni-N-C, Fe-N-C and N-C were tested in a flow reactor achieving partial current densities for CO above 200 mA cm^{-2} [33]. For the production of HCOOH, this family of catalysts has to the best of our knowledge not been studied yet in flow reactors. However, *Peng et al.* recently achieved high formate selectivity (90%) at 15.6 mA cm^{-2} using bimetallic Cu/Sn embedded in a nitrogen-doped carbon cloth, evidencing the promising nature of Sn [34].

Although multiple reports of selective M-N-C catalysts for CO and HCOOH production already exist, little attention has thus far been paid to its performance at industrially relevant current densities. Consequently, a very limited number of accounts in literature report tests of this family of catalysts in continuous flow reactors [33,35,36]. For industrial applicability, the energy efficiency, current density and stability still have to increase. According to *Kibria et al.*, the performance requirements stand at current densities above 300 mA cm^{-2}, Faradaic efficiency above 80%, cell voltage lower than 1.8 V and stable operation for more than 80 000 hours [37]. Therefore, focus on the reduction of the cell voltage at high current densities while achieving high stabilities is of utmost importance.

In this work, different transition metals (nickel, cobalt, iron, manganese, tin) embedded in nitrogen-doped porous carbons have been analyzed under identical conditions in a continuous flow cell at industrially relevant current densities (up to 200 mA cm^{-2}) as alternative for precious metal catalysts for the ERC. This study constitutes an unprecedented analysis of this family of catalysts using a gas diffusion electrode as such preventing the influence of CO_2 supply limitation ever-present in aqueous phase testing. The role of the transition metal incorporated into the catalyst on the selectivity, activity and stability was analyzed by minimizing the

variability of the synthesis method, down to the metal that is incorporated. Electrochemical performance was linked to a physicochemical study that encompassed a multitude of characterization techniques such as N_2 physisorption, XPS, ICP-MS and Raman spectroscopy. Our results evidence the high productivity and stability of Ni-N-C and Sn-N-C and its significant advantages over other M-N-C and commercial Ag nanoparticles.

2. Experimental

2.1. Materials

The chemicals used to synthesize the M-N-C were aniline (99.8%, Acros Organics, Belgium), manganese chloride (>99%, Sigma Aldrich, Belgium), cobalt chloride hexahydrate (>97%, Sigma Aldrich, Belgium), nickel chloride hexahydrate (99.9%, Sigma Aldrich, Belgium), iron(II) chloride tetrahydrate (>99%, Sigma Aldrich, Belgium), tin chloride dihydrate (>99.99%, Sigma Aldrich, Belgium), ammonium peroxydisulphate (>98%, Fluka, Belgium). The chemicals used for the electrochemical analysis were potassium bicarbonate (>99.5%, Chem-Lab, Belgium), CO_2 (99.998%, Nippon, Belgium), potassium hydroxide (85% assay, Chem-Lab, Belgium), Nafion® suspension (5 wt% in lower aliphatic alcohols and water, Sigma Aldrich, Belgium) and isopropanol (>99%, Chem-Lab, Belgium). Ultrapure water was prepared in the laboratory (Milli-Q gradient, Millipore, USA). The Nafion® 117 membrane was purchased from Fuel Cell store (USA).

2.2. Synthesis of M-N-C

The different M-N-C were synthesized utilizing similar methods, previously developed in our group, via the pyrolysis of activated carbon, aniline and metal precursors [32]. Norit® activated carbon (AC) was on a first step subjected to a 6 M HCl aqueous solution for 24 h at room temperature to remove impurities and subsequently immersed in 0.5 M (<10 °C). After 15 min, 2.5 mL of aniline was added. In order to polymerize the aniline, ammonium peroxydisulphate (APS) $(NH_4)_2S_2O_8$ was added after 1 h (1.2:1 APS to aniline molar ratio), simultaneously with the metal precursor in a 1:1 metal to aniline molar ratio (except for N-C and Sn-N-C). Next, the mixture was stirred for 24 h while the temperature was kept below 10 °C. Afterwards, the solvent was evaporated using a Büchi rotavapor and the remaining solid further dried in an oven at 100 °C overnight. The powder was subjected to two pyrolysis steps under Ar, the first for 1 h at 900 °C with a ramp of 3.3 °C min^{-1} and the second one for 3 h at 900 °C. In between the two pyrolysis steps the powder was treated in a reflux setup with 0.5 M sulphuric acid for 8 h to remove unstable (metal) species, filtered, washed with deionized water and dried overnight at 100 °C. Since the method described above resulted in inferior Sn-N-C electrocatalysts (2.73 wt% surface Sn as measured by XPS), producing no formic acid at all in a H-cell (Figure S4). Since this in contrast to the known literature on Sn, we decided not to consider this electrocatalyst for flow-cell experiments but instead try to improve this initial performance by altering the synthesis method but keeping a similar supporting material (namely N-doped carbon). As such we hoped to introduce more active Sn sites and to this end we added Sn through a vacuum impregnation post-synthesis method, incorporating the metallic species in its

most active form, which for Sn-N-C is expected to be M-O_x instead of the M-N_x. In this case, metal-free N-doped carbon was synthesized following the procedure described above (but in the absence of a metal precursor) and was used as a support for vacuum impregnation. In short, 200 mg synthesized metal-free support was mixed with 800 µL of 0.66 M aqueous solution of $SnCl_2.(H_2O)_2$ under vacuum for 3 min and dried overnight in an oven. Afterwards the material was annealed at 300°C for 1h under Ar, followed by a reduction under 5% H_2 in Ar with the following temperature program: 10°C min^{-1} to 450°C for 1h and 20°C min^{-1} to 600°C for another hour.

2.3. Physicochemical characterization

The different metal-nitrogen-doped carbons were investigated using a set of physicochemical characterization techniques. Firstly, in order to determine its metallic weight percentage, the impregnated carbon powders were analyzed using an Agilent 7500 series inductively coupled plasma mass spectrometer (**ICP-MS**). 10 mg sample was dissolved in 500µL of aqua regia and destructed at 70°C overnight. The samples were diluted to a 1:100 ratio and a calibration curve was fitted from 100 to 10 000 ppb. Standards for all metallic species analyzed were purchased from VWR (Belgium). Then, the chemical analysis of the catalyst surface composition was conducted using X-ray photoelectron spectroscopy (**XPS**). These measurements were performed by a Physical Electronics PHI 1600 multi-technique system using an Al Kα (1486.6 eV) monochromatic X-ray source, which was operated at 15 kV and 150 W at a base pressure of $2 \cdot x10^{-9}$ Torr. The graphitic C 1s band at 284.6 eV was taken as internal standard, in order to correct possible deviations caused by electric charging of the samples. The MultiPak software

was used for the deconvolution and integration of the XPS signals. In order to obtain information on the catalysts degree of graphitization, room-temperature **Raman** spectra were recorded making use of a LabRAM HR Evolution spectrometer from HORIBA Scientific. The spectroscope was equipped with a high stability confocal microscope with XYZ motorized stage and objectives of 10x, 50x and 100x magnification, a multichannel air cooled detector (with a spectral resolution smaller than 1 cm^{-1}) and a solid state laser at a wavelength of 532 nm (Nd:YAG). Deconvolution and peak integration was performed using the IgorPro software. With the aim of verifying the porosity and specific surface area of the samples, we utilized **N_2 physisorption**. Nitrogen adsorption-desorption isotherms were measured at 77 K on a Quadrasorb SI from Quantachrome. The pore size distributions were determined using the Barrett-Joyner-Halenda (BJH) method, whereas the Brunauer-Emmett-Teller (BET) method was used to calculate the surface area of the samples. Next, with the aim of characterizing the crystalline structure of the catalysts, X-Ray diffraction (**XRD**) was employed. A STOE Stadi P Combi instrument was used in transmission mode to measure the X-ray diffraction patterns. The instrument was used in high-throughput mode and was equipped with a Cu-Kα radiation source (λ = 1.54 Å) and a Kα1 Germanium Johann-type monochromator. A high-throughput image plate position detector (IP-PSD) from STOE was used as detector. The XRD instrument was controlled by WinXPOW version 2.20 software from STOE and all the measurements were performed in the 2θ range from 0 to 75°. Subsequently, scanning Electron Microscopy and Energy-dispersive X-Ray Spectroscopy (**SEM-EDX**) were used in order to assess the homogeneity of the distribution of the metal species and to identify metallic clusters. The microscope used was a Quanta 250 FEI operated at 20 kV using secondary electrons. Finally, a Thermo Fisher Scientific Themis Z electron microscope equipped with a Gatan 977 Enfinium

EELS spectrometer and a Super-X EDX detector was used to study the morphology of the obtained catalysts and verify the atomic distribution by **EDX** and **EELS**.

2.4. Electrochemical analysis

All electrochemical measurements were carried out in an adapted micro flow cell of ElectroCell (Denmark), allowing to operate in a three-electrode flow-by mode (Figure S1). A detailed description can be found in previous work [38]. A 10.2 cm² gas diffusion electrode (Sigracet® 39BC, Fuel Cell Store) was used as cathode. An ink consisting of catalyst, Nafion suspension, isopropanol and milli-Q® water was sprayed onto its microporous layer, until a loading of 2.0 mg cm-2 was reached. The w:w ratio of Nafion:catalyst in the ink was optimized to 1:7 (Figure S5) and the volumetric ratio water:isopropanol was 1:3. The ink was ultra-sonicated for 25 minutes prior to airbrushing. The cathodic potential was controlled versus a leak-free Ag/AgCl reference electrode (Innovative Instruments, Inc.) with a multichannel Autolab potentiostat M204 equipped with an FRA module and a 10 A booster. The measured potentials were converted to the RHE reference scale and corrected for an ohmic resistance between working and reference electrode of 0.55 ohm via the eq. 1.

$$E\ (V\ vs\ RHE) = E\ (V\ vs\ Ag/AgCl) + 0.059\ \times pH + 0.21 - R \times I \qquad (1)$$

CO_2 flow rate was controlled with a Brooks Instrument GF-40 mass flow controller and was fed to the GDE at a constant rate of 40 sccm. The catholyte and anolyte used were respectively 0.5 M aqueous KHCO3 and 2 M aqueous KOH. In both the flow rate was kept at 20 mL min-1 with a multichannel peristaltic pump. A Nafion® 117 cation exchange membrane separated the two compartments. The system was operated in recirculation mode as shown in Figure S2 and

the electrolyte volumes were 250 mL for the potential screening experiments and 1000 mL for the stability tests. The gaseous stream was separated from the liquid and directed to an in-line Shimadzu 2014 series gas chromatograph equipped with a TCD detector and a micropacked column (Restek Shincarbon ST, 2 m length, 1 mm internal diameter, 100/120 mesh). For the potential screening experiments (duration of 45 min), two gaseous samples were analyzed at 20 and 40 minutes. For the stability tests, gaseous samples were analyzed every 20 minutes throughout the entire measuring period. The liquid phase was analyzed with an HPLC (Alliance 2695, Waters, USA) combined with a packed column (IC-Pak, Waters, USA) and a PDA detector (2996, Waters, at 210 nm) to quantify the amount of formate present in the catholyte at the end of each experiment and intermittently for the stability experiments. A perchloric acid solution (0.1%) was used as the eluant for the HPLC analysis. Prior to analysis, 1 mL samples were acidified with 200 µL perchloric acid 6 M solution, sonicated and finally filtered.

3. Results and Discussion

3.1. Physicochemical characterization

M-N-C catalysts were synthesized with different embedded metal species (Sn, Co, Fe, Mn and Ni) with the purpose of identifying the role of the metal on the activity, selectivity and stability under industrially relevant conditions. Herein its performance is linked to material properties through a combination of physicochemical and electrochemical characterization techniques. N_2 physisorption was used to analyze sample porosity and surface area. Based on the Brunauer–

Emmett–Teller method (BET), the surface area was determined which ranged from approximately 450 (Mn-N-C) to 850 $m^2 g^{-1}$ (Co-N-C) (Table 1). As the synthesis procedure was simillar for all M-N-C, this indicates a higher ability of Fe-N-C and Co-N-C in generating nanoporous structures. The higher metallic content in Sn-N-C sample is believed to compromise its porosity due to the non-porous character of metallic species, leading to S_{BET} values close to those of Mn-N-C, which performed poorly in generating nanoporosity. The analysis of the N_2 adsorption-desorption isoterms (Figure S6) revealed an increase of nitrogen uptake at higher relative pressures, indicative for a high mesoporosity, confirming good accessibility to the active sites. Notably, the incorporation of metals decreased the pores dimensions for all M-N-C (3.4 nm in N-C in opposition to 2.0 nm of Ni-N-C, Sn-N-C and Mn-N-C), indicating their presence also inside of the carbon support, suggesting a homogeneous distribution of the metals and thus the active sites.

Next, in order to obtain information on the degree of graphitization of the samples, Raman spectroscopy was used. The spectra (Figure S7) showed the characteristic D band around 1350 cm^{-1} (indicative of disordered carbon structures) and G band at about 1600 cm^{-1} (indicative of the presence of ordered graphitic carbon)[29,39]. Based on the ratio of the areas of these two peaks and on the width of the D band, we can conclude that Co-N-C reveals the highest level of graphitization followed by Ni-N-C and Fe-N-C, which goes in line with previous studies that report the beneficial role of these metal species in promoting the graphitization [40]. The Sn-N-C spectrum indicated the lowest level of graphitization, which is straightforward as Sn was incorporated post-synthesis and can thus not promote graphitization. On the contrary, its incorporation tends to lower graphitization through the formation of additional surface defects. Two other peaks are discernible after deconvolution at 1200 cm^{-1}, characteristic of C atoms

outside of its sp^2 plane, and 1500 cm^{-1}, indicative of the presence of doped heteroatoms such as nitrogen.

Table 1. Surface area based on BET method, pore size, surface elemental composition, ICP-MS metallic content analysis and degree of graphitization of M-N-C and N-C.

	Physisorption		XPS				ICP-MS	Raman	
Sample	**S_{BET} (m^2 g^{-1})**	**Pore size (nm)**	**Wt% C**	**Wt% N**	**Wt% O**	**Wt% M**	**Wt% M**	**A_D/A_G**	**FWHM (D-band)**
N-C	763	3.4	86	7.2	2.8	/	/	1.1	130
Co-N-C	842	2.5	81	2.1	6.2	4.5	18.2	0.9	110
Fe-N-C	827	2.6	78	7.6	11	3.2	7.2	1.0	125
Mn-N-C	451	2.0	87	4.5	7.0	1.1	2.5	1.1	130
Ni-N-C	772	2.0	92	1.6	2.6	1.3	1.8	1.0	121
Sn-N-C	514	2.0	44	2.3	13.4	40.2	8.8	1.2	154

X-ray photoelectron spectroscopy (XPS) was used in a next step to determine surface elemental composition and configuration of surface atoms. The incorporation of nitrogen atoms in the carbon matrices resulted in an N weight percentage ranging between 1.6 and 7.6%. The formation of metal-nitrogen bonds is more likely than metal-carbon or metal-oxygen and leads to higher energy stability. In order to verify the presence of $M\text{-}N_x$ complexes and pyridinic N (as

potential active sites for ECR), the high resolution N 1s spectra were deconvoluted and analyzed (Figure S8 and Table S1). The N spectrum showed a peak for metal-coordinated species ($M\text{-}N_x$ at 399 eV) for all metal species, in addition to peaks for pyridinic N (N1, 398.7 eV), pyrrolic N (N2, 400.0 eV), graphitic N (N3, 401.5 eV) and oxidized pyridinic N (N4, 402.4 eV). All spectra were dominated by a combination of graphitic and pyridinic nitrogen moieties. The graphitic N prevalence was more accentuated in the Sn-N-C, which contrasts to its lower carbon graphitization determined with Raman spectroscopy, Ni-N-C and Co-N-C, while in Fe-N-C there was a higher formation of pyridinic functionalities. Mn-N-C revealed an equilibrium between the two dominant moieties. The pyrrolic and oxidized pyridinic functionalities seemed to be less abundant, which is logical. Indeed, while the former is proven to be less resistant to high pyrolysis temperatures (>700°C), the latter is only formed due to exposure to air of N1. Due to overlap with N1 and N2, the $M\text{-}N_x$ moiety was more difficult to quantify, especially for the electrocatalysts whose metal preferred higher oxidation states such as Sn-N-C and Mn-N-C. The presence of these higher oxidation states may be representative of only the surface of the electrocatalysts, triggered by oxygen adsorbates unavailable in the bulk of the M-N-C. Deconvoluting the O1s spectra revealed the presence of MeO_x species in addition to the carbon-bound oxygen species typically found in this type of carbon materials (Figure S9). By combining the relative fraction of metal oxides present in the O1s spectrum with the relative oxygen and metal contents, the fraction of metal oxides present at the surface can be estimated. For Co, Fe, Mn and Ni the remaining fraction is then considered to be $M\text{-}N_x$ species as no metallic (or other) species could be detected with XPS (and XRD). For Sn the remaining species were assigned to metallic Sn species as a certain fraction of the deconvoluted Sn 3d XPS spectrum could be assigned to metallic Sn. As such relevant quantities of $M\text{-}N_x$ especially in Ni-N-C, Co-N-C and

Fe-N-C (0.90 %, 1.62% and 2.69%, for more detailed information on the calculation see SI) were revealed.

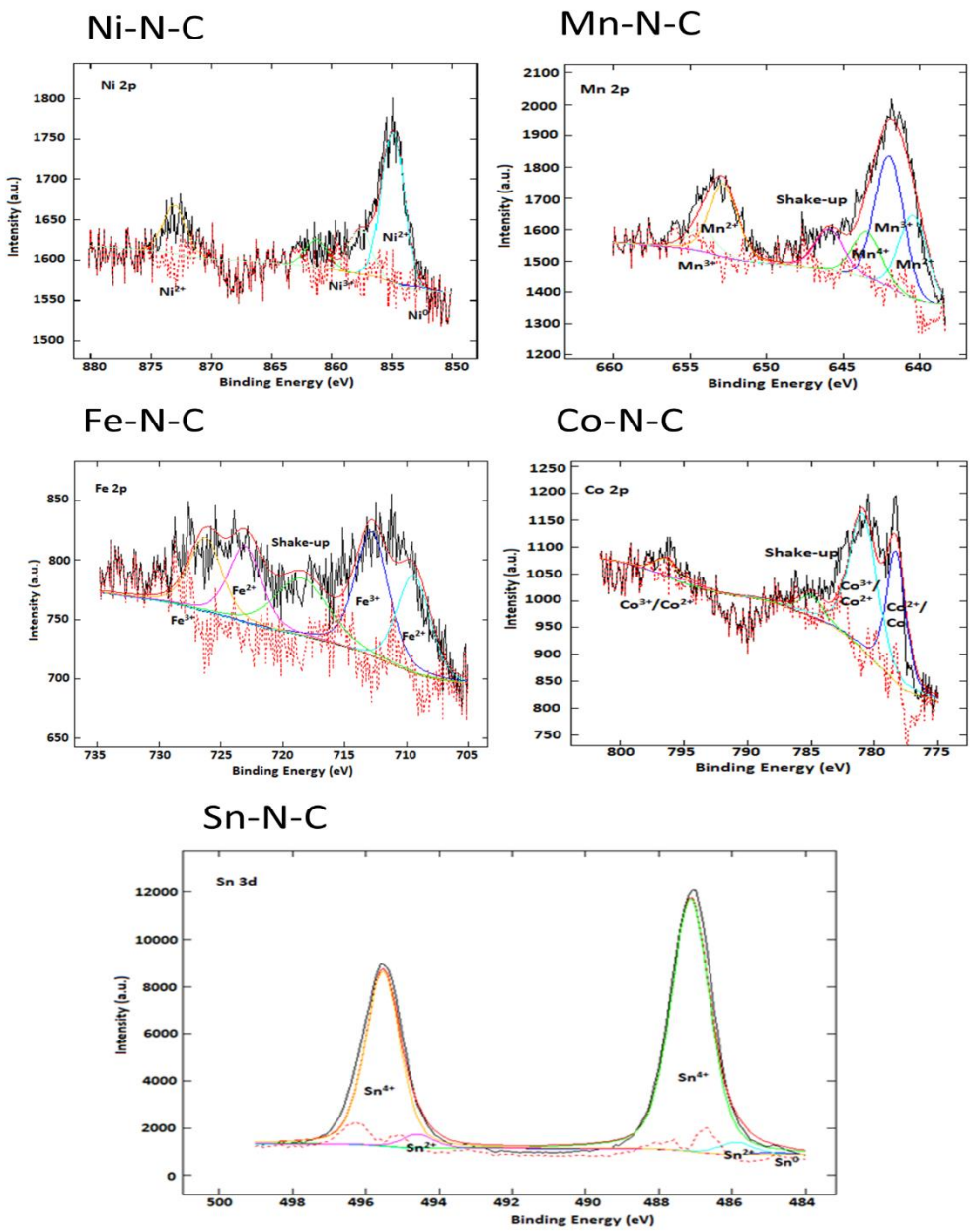

Figure 1. Deconvoluted 2p and 3d XPS spectra of M-N-C

High-resolution metal 2p XPS spectra of M-N-C were further deconvoluted to analyze the chemical states of the metallic elements (Figure 1). Different oxidation states for the metals incorporated were visible for all M-N-C, indicative of topological heterogeneity of the M-N_x moieties. The fitted Ni $2p_{3/2}$ spectra shows a large peak at 855 eV, which can be deconvoluted in three peaks associated to Ni^0, Ni^{2+} and Ni^{3+}. The peak at 854.8 eV (Ni^{2+}) in combination with the shake-up peak suggests the presence of Ni-N, which is confirmed further on by STEM-EELS measurements. The Fe spectrum reveals the coexistence of Fe^{2+} and Fe^{3+} with peaks at 709.4 eV and 712.7 eV. This could be indicative of oxide peaks (FeO and Fe_2O_3) but also of Fe-N moieties as already detected in the Fe-N-C N 1s spectrum and confirmed with STEM-EELS. Fe $2p_{1/2}$ peaks at 721.4 eV and 725.2 are also visible. The photoemission lines of the Mn 2p spectrum are dominated by a peak at 641.5 eV, which indicates a predominance of Mn^{2+}, Mn^{3+} and Mn^{4+} species. Because M-N_x moieties were only scarcely detected in its N 1s spectrum and a large metal oxide peak was found in the O1s spectrum, these are all assigned to oxide species, which may be indicative of a lower stability of this catalyst (as oxides tend to reduce under the reductive environment during reaction). The Sn 3d spectrum reveals the presence of metallic Sn, Sn^{2+} and Sn^{4+} at binding energies of 485.0 eV, 486.0 eV and 487.1 eV, which has been found in literature to correspond to Sn, and SnO_2 species respectively. The predominance of SnO_x, suggested by large Sn^{2+} and Sn^{4+} peaks, was confirmed resorting to deconvoluted XPS O 1s spectra (Figure S9, vide supra). The Co $2p_{3/2}$ spectrum indicates the presence of metallic Co, Co^{2+} and Co^{3+}, which can be assigned to both cobalt oxides and/or Co-N_x species. The joint

analysis of Co $2p_{3/2}$ and N 1s spectra reveals 64% of oxide species and 36% of Co-N_x species. However, these metal sites may change to more reduced states during ERC as *Li et al.* determined using XANES spectroscopy before and after electrochemical operation [41]. The metallic content in the M-N-C was finally also determined through inductively coupled plasma mass spectrometry (ICP-MS) (Table 1). Co-N-C gave the highest metallic content (18.2%), followed by Sn-N-C (8.8%) and Fe-N-C (7.2%). The M-N-C with the lowest metallic content indicated a Ni presence of 1.8%. The variation between the metallic weight percentage gathered from ICP-MS and XPS is attributed to the latter being a surface analysis technique which has a detection depth inferior to 5 nm [42], therefore not taking into account the underlying N-doped carbon layers. The embedding of Sn via post-synthesis vacuum impregnation resulted in a higher percentage of surface metal. The catalysts were still structurally characterized using X-Ray Diffraction (XRD). Ni- and Mn-N-C revealed an amorphous structure besides the broad peak around 25° caused by the graphitic carbon, while the main peaks of Sn-N-C are assigned to crystalline SnO_x (Figure S10). The spectra for Co- and Fe-N-C reveal the presence of also sulfide peaks, which find its origin in the use of APS as oxidant. They are however, expected to not be active towards the CO2RR as they are believed to be mainly present in the bulk of the material and not present at the surface.

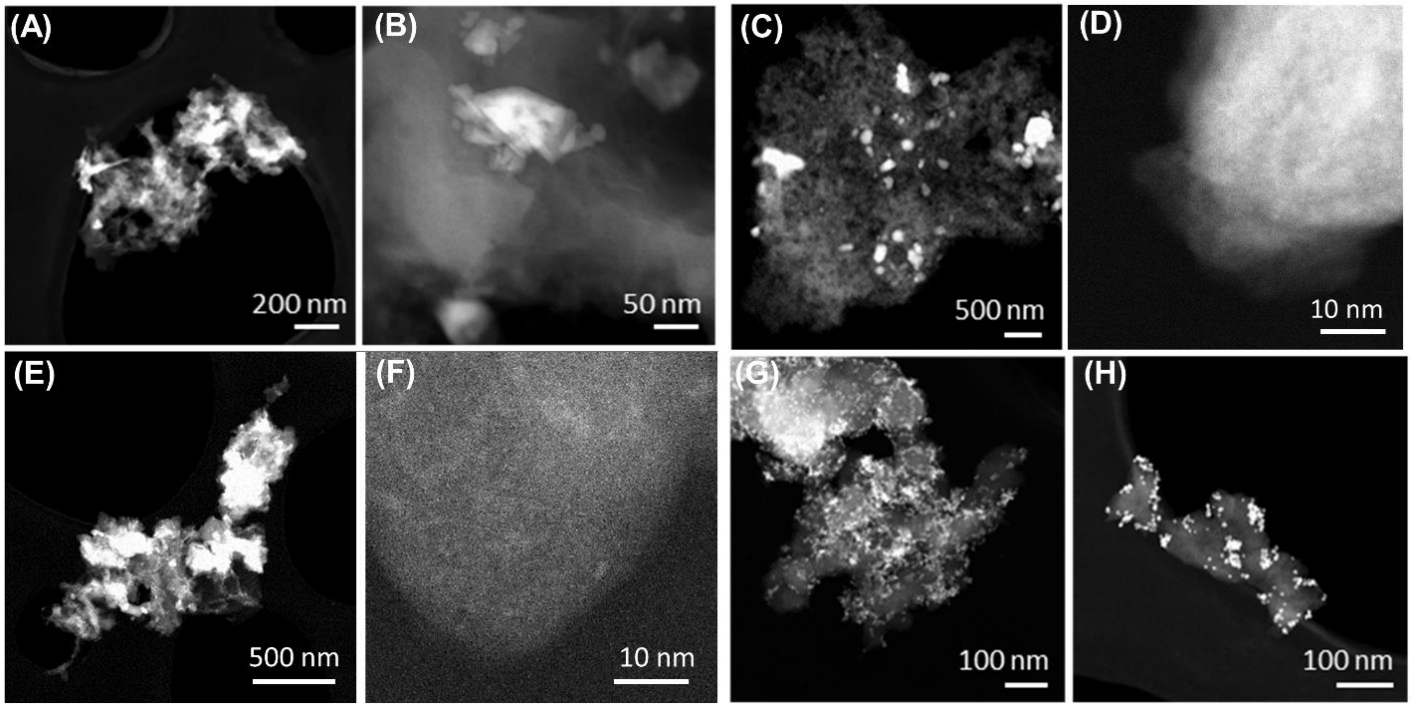

Figure 2. (A-B) TEM images of Mn-N-C. (C) Fe-N-C TEM image and (D) HAADF where the presence of nanoclusters and possibly single atoms can be detected as bright spots along the C-N support. (E) Co-N-C TEM image and (F) HAADF where bright point contrast suggests the presence of nanoclusters and possibly single atoms. (G-H) TEM images of Sn-N-C showing homogeneous distribution of small nanoparticles (6-7 nm).

In order to evaluate the homogeneity of the distribution of metallic species in the carbon framework EDX analysis was performed for each sample (Figures S13-16), revealing a high level of homogeneity in the distribution of the metallic species in the N-doped carbon support. As expected, Sn formed small oxide nanoparticles (6-7 nm) homogeneously distributed over the support. Fe and Ni (the latter being analyzed in our previous work[43]) were dispersed in the form of small oxide nanoparticles and possibly single-atom sites. As for Co-N-C, Co is distributed in the form of oxide nanoparticles with heterogeneous size. The HAADF-STEM

images of Mn finally show a distribution of oxide nanoparticles of different sizes corroborating the XPS spectrum which suggested the dominance of Mn-O_x species. Finally, in an attempt to confirm the successful formation of single atomic metallic sites, high resolution HAADF-STEM imaging was used as this allowed distinguishing heavier metallic elements from the N-doped carbon. Clusters in the nanometer range or smaller were detected for Ni-N-C (previously published[43]), Co-N-C and Fe-N-C. In our previous publication, these clusters were assigned to Ni by the presence of a clear Ni L_{23} edge visible with EELS.[43] Similarly, Co and Fe L_{23} edges were detected in this work (Figures S11 and S12) establishing the composition of the nanoclusters as Co and Fe, respectively. These results corroborate the XPS analysis suggesting the formation of M–N_x functionalities for these catalysts. No single-atom Sn and Mn was detected for the obtained catalysts.

In conclusion, this combination of physicochemical characterization techniques reveals how the incorporation of different metal species in nitrogen-doped carbon gives way to different characteristics for each M-N-C. The embedding of nitrogen and metallic atoms in graphitic structures was successful as well as the formation of a nanoporous structure. While surface Ni and Fe were incorporated mostly in its M-N_x form, oxides species were predominant for surface Sn, Co and Mn, although not exclusively.

3.2. Electrochemical performance

Electrochemical measurements were performed at controlled cathodic potentials in a first step. Figures 3 and 4 respectively depict the Faradaic efficiencies and current densities achieved for each potential. All cathodic potentials are reported versus the reversible hydrogen electrode (RHE).

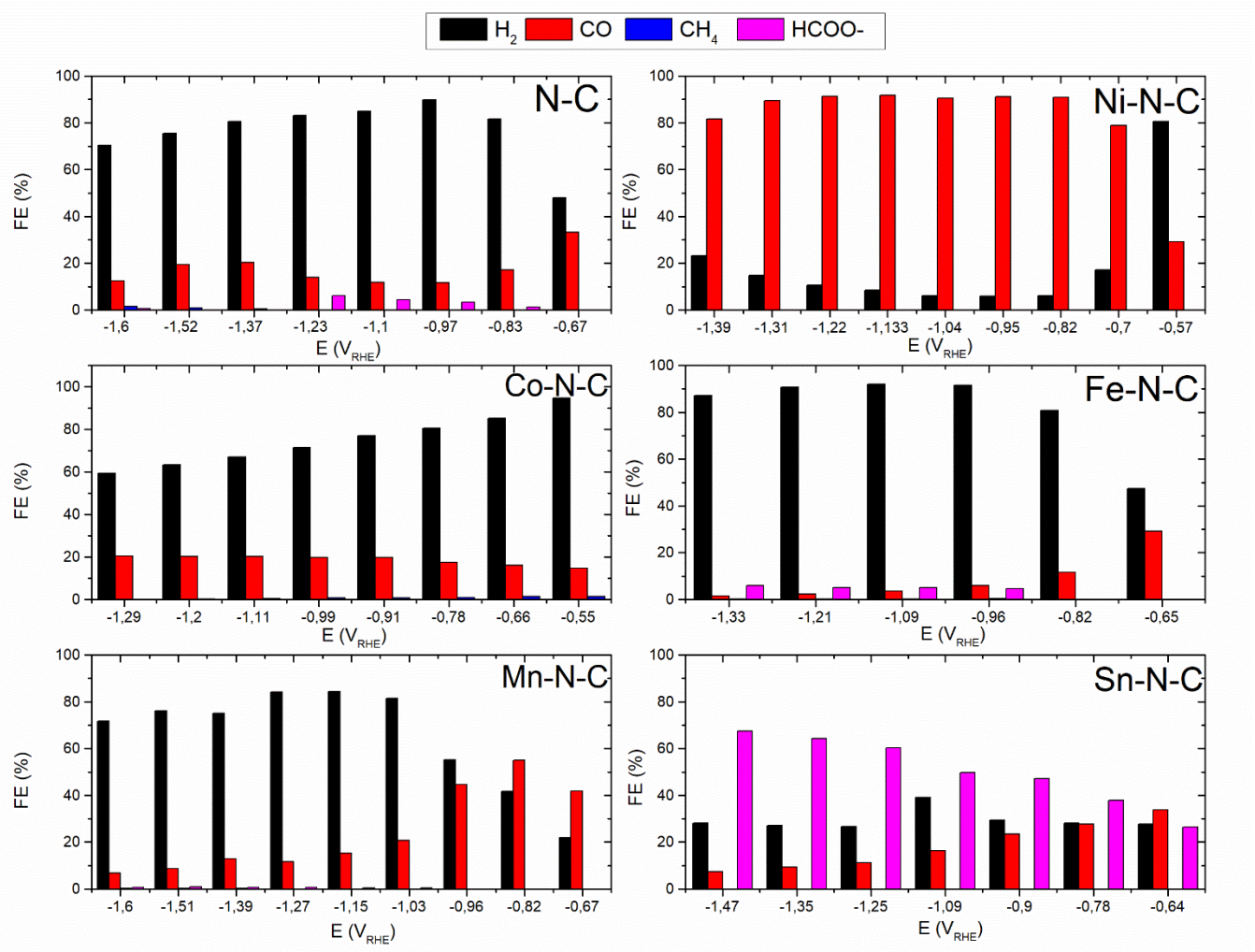

Figure 3. Selectivity profile of the obtained catalysts.

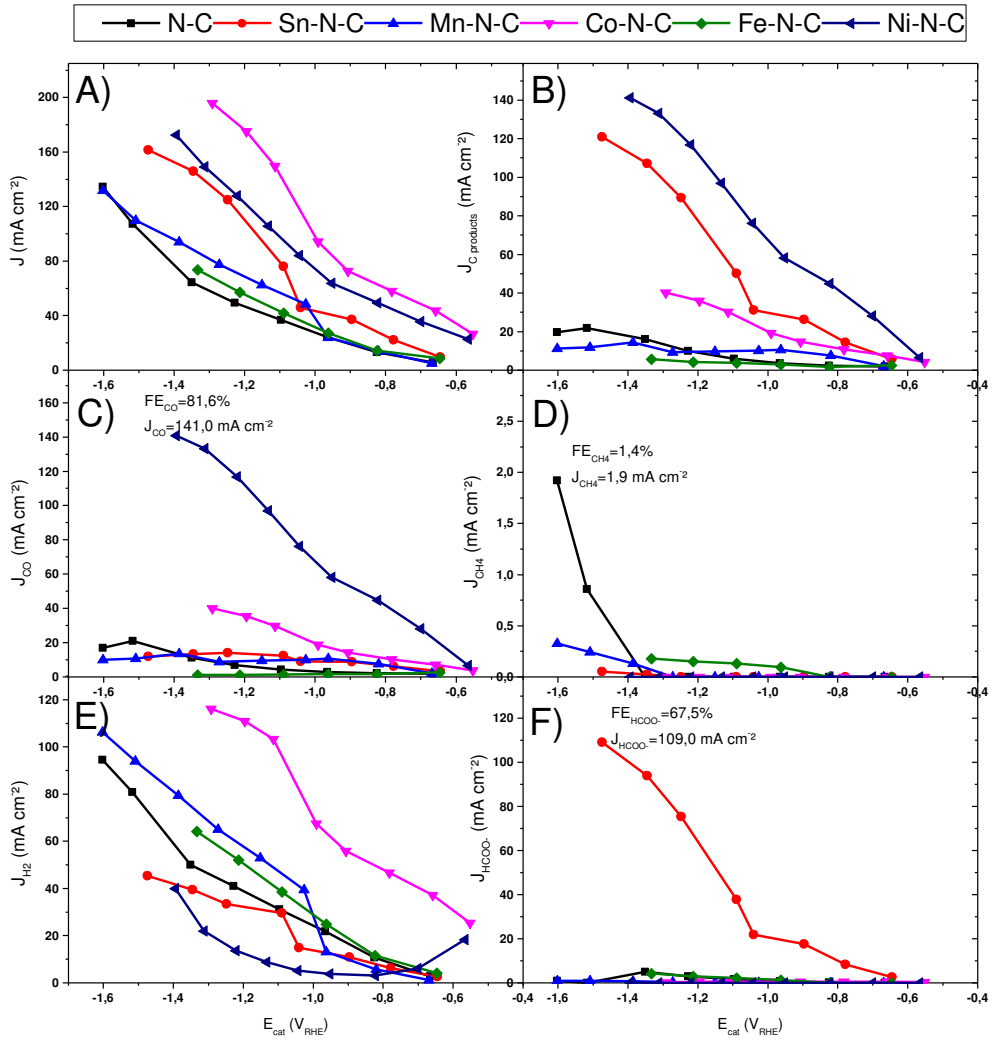

Figure 4. Metallic species influence on catalyst activity; A) Total current density; B) Partial current density towards ERC products; C) Partial current density towards carbon monoxide; D) Partial current density towards methane; E) Partial current density towards hydrogen; F) Partial current density towards formate.

Overall, the incorporation of metals in the N-doped carbon resulted in higher catalytic activity compared to the activity of the metal-free electrocatalyst. Furthermore, the differences in catalytic behavior with the inclusion of different metals can be rationalized in terms of the variation in binding energies for H*, CO_2^-* and CO*, which in turn are correlated to the number of d-antibonding electrons of the metallic species [41]. Co-N-C led to the highest reactivity achieving the highest current densities. From Figure 4-F we can already highlight the performance of Ni-N-C and Sn-N-C for the production of carbon products. Throughout the whole range of potentials, the catalyst with nickel as active site largely outperformed the other electrocatalysts for the production of CO achieving 141 mA cm^{-2} at -1.39 V, corresponding to a productivity of 589 L $m^{-2}h^{-1}$. The low binding energy for CO* of the Ni-N_x moieties prevents a CO desorption limitation and the weak H* affinity of most NiN_x coordinative states makes the catalyst able to suppress HER even at high overpotentials [44]. The first electron transfer is therefore the rate-determining step. Manganese and iron active sites exhibit moderate selectivities at low overpotentials, characteristic of its low COOH* binding energy, though achieving modest current densities. At cathodic potentials more negative than -0.5 V_{RHE}, Fe^{+3}-N_x species are known to reduce to Fe^{+2}-N_x, which catalyze the ERC less effectively due to their stronger CO binding[45,46]. Sn-N-C stands out for being the only catalyst able to reduce CO_2 to formate at a high rate up to 109 mA cm^{-2} at -1.47 V, which corresponds to a productivity of 751 g $m^{-2}h^{-1}$. Its high activity is attributed to the abundance of active sites due to a high metallic content and richness of surface defects on the N-doped carbon. On one side, the nitrogen-doped carbon support contributes with high CO_2 adsorption properties and high conductivity enhancing the electron transfer steps. On the other, SnO_2, which is believed to be the main active site, has a higher affinity to the O atoms and catalyzes formate production by protonating the adsorbed

CO_2^-, via the *OCHO intermediate (see reaction pathway in Figure S4). Operation with Co-N-C leads to the preferential HER pathway due to its high binding energy with H*, limiting $FE_{C\ products}$ to a maximum of 22.4% at -1.11 V. This unfavorable H* binding energy is related to the protonation of Co-N_x species and consequent formation of Co hydride intermediates[47]. Furthermore, superficial Co is mainly in its oxide form as well as in its sulfide form as detected in XPS and XRD spectra respectively, while Co-N_4 species are reported to be the most active for CO_2 reduction [48]. Despite its high CO_2^{-*} binding energy and its large partial current density towards CO (Figure 4-C), its low selectivity results in high energy requirements thus limiting its applicability. In Figure 4-D we denote a high onset potential for the formation of methane for Mn-N-C (-1.39 V) and N-C (-1.37 V) in contrast to the low onset potential of the Fe-N-C (-0.96 V), making this a rare report of non-Cu based catalysts that reduce CO_2 to hydrocarbons. The fact that these catalysts are able to produce hydrocarbons is related to its higher CO* binding energy, which allows the molecule to be further reduced. However, this leads to a desorption limiting step, which in turn limits the turnover frequency of CO. Consequently, the productivity of CO is lower for these catalysts despite larger metallic contents in comparison to the Ni-N-C sample. The relevance of the nitrogen functionalities cannot be excluded. In fact, the metal-free catalyst outperformed Fe-N-C (and Mn-N-C at very negative cathodic potentials) in terms of productivity of carbon products. This may be related to the aggregation of Fe and Mn metallic and oxide clusters which is known to catalyze the HER [41,49]. In opposition to Sn-N-C, which has its main active site in the M-O_x species, the presence of oxides is undesirable in both Fe-N-C and Mn-N-C, the main active sites of which are the M-N_x moieties. Interestingly, a high degree of similarity in Faradaic efficiencies is observed when comparing these results to previous M-N-C reviews in batch reactors such as the one carried out by *Ju et al*. We can conclude that by

moving towards a flow reactor and including a gaseous CO_2 feed, the current density was successfully increased while at the same time maintaining high selectivity. This clearly evidences the benefits of using a three-phase interface in avoiding mass transfer limitation and thus CO_2 depletion, which limits current densities in a typical batch cell due to low CO_2 solubility.

In order to evaluate the overall reactor performance, the oxygen evolution in alkaline media counter reaction was monitored as well. The cell potentials ranged from 2.3 V to 5.3 V from low to high current densities (Figure S17). This allowed calculating the energy efficiency of the electrolyzer, utilizing the following equation (2):

$$\varepsilon = \frac{\text{FE x } E_k^0}{E_{cell}} \qquad (2)$$

Where E_k^0 is the equilibrium cell potential for the product studied, which is -1.35 V for CO and -1.49 V for $HCOO^-$. The operation with Ni-N-C reached its maximum CO energy efficiency of 41.5% at E_{cat} = -0.82 V (see Figure 5). Sn-N-C showed a $HCOO^-$ energy efficiency peak at E_{cat} = -0.90 V with a value of 23.2% (with a simultaneous ε_{CO} of 10.4%).

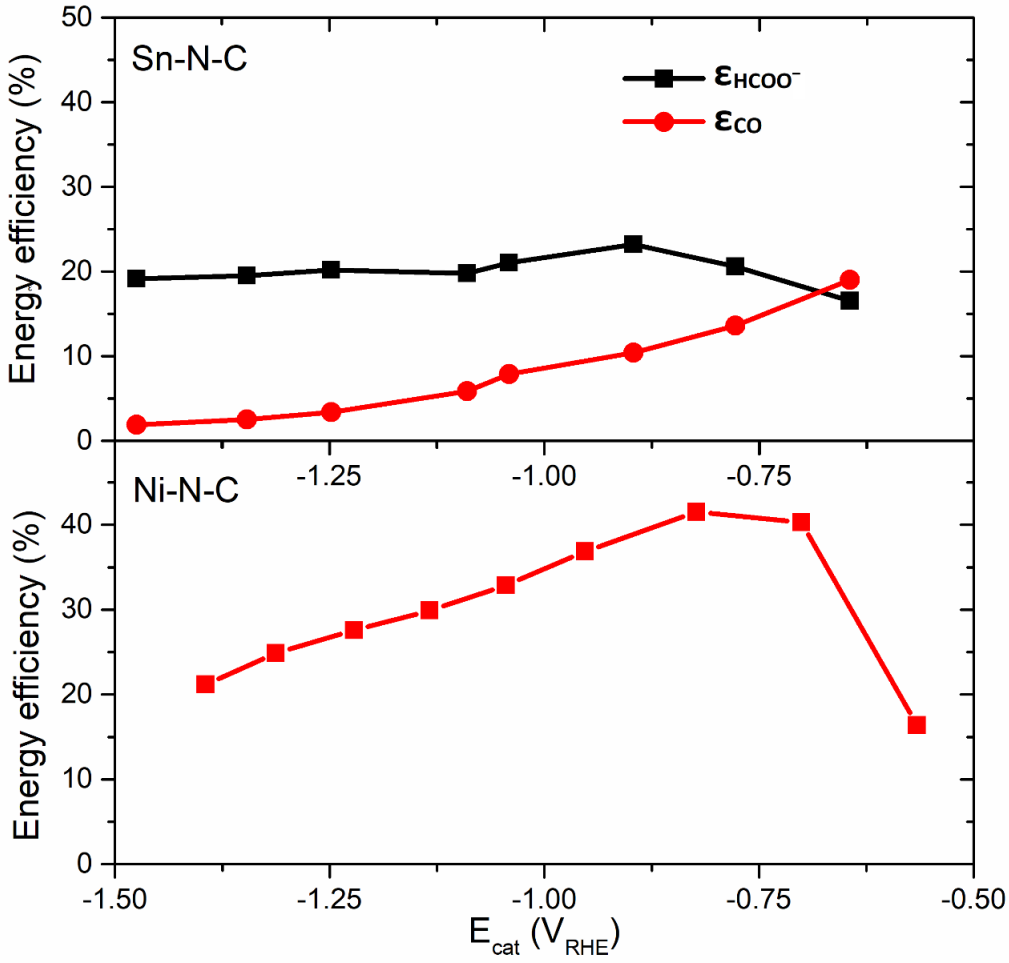

Figure 5. Cell energy efficiency for Sn-N-C and Ni-N-C.

Since the metallic species play an important role in the reaction pathway and the metallic content in the electrocatalysts varies (from 1.8 wt% of nickel to 8.8 wt% of tin), a turnover frequency (TOF, h^{-1}) study was performed. TOF for carbon dioxide reduction per metallic site is defined as the mole of CO_2 reduction product formed, divided by the mole of transition metals in the M-N-C. It was calculated based on the equation 3:

$$\mathrm{TOF} = \frac{n_{C\ product}}{n_{metal}} = \frac{M * n_{C\ product}}{m * x_m} \qquad (3)$$

Where M is the atomic mass of the metal (g mol^{-1}), m is the catalyst loading of the electrode (g cm^{-2}), x_m is the metallic percentage of the catalysts mass, and $n_{C\ product}$ is the ERC productivity in mol cm^{-2}h^{-1}. Metallic mass percentages obtained via ICP-MS were, on a first step, used to obtain accurate metallic turnover frequencies. On a second step, in order to take into account the accessibility of metallic sites, turnover frequencies were calculated using the surface metallic composition, $x_{m,s}$, and BET surface area, S_{BET}.

$$\mathrm{TOFn} = \frac{M * n_{C\ product}}{m * x_{m,s} * S_{BET}} \ (4)$$

Ni-N-C was confirmed as the most suitable catalyst due to the combination of high activity and low metallic content (Figure 6-A). Co-N-C, which operated at high activity and moderate selectivity to CO, had uninteresting turnover frequencies due to its high metallic content. Mn-N-C showed low reactivity at all potentials, only higher than Fe-N-C, which had high metallic content and low productivity. However, Figure 6-B indicates that Mn-N-C performance may be limited by a lower availability of active sites due to a lower porosity and metallic content. This led to the second highest normalized TOF, reaching an ERC productivity of 454 mmol m^{-2}h^{-1}. Operating at the highest productivity of ERC products, Sn-N-C had a TOF of 1522 h^{-1} ($FE_{C\ products}$ = 74.9%), while Ni-N-C had a TOF of 4292 h^{-1} ($FE_{C\ products}$ = 82.7%), which represents a twofold increase by comparison with *Pan et al.* review of M-N-C [28]. The turnover frequency analysis normalized by the respective BET surface area-weighted surface metallic concentration achieves a maximum of 2623 mmol m^{-2}h^{-1} with Ni-N-C representing an improvement by two orders of magnitude by comparison with the study of *Ju et al.* [50].

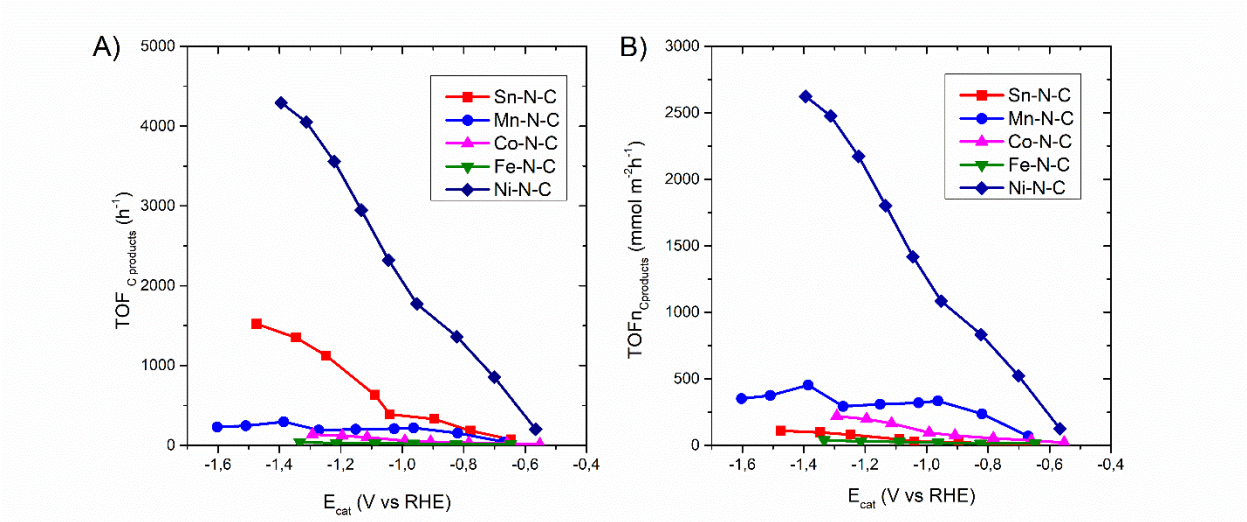

Figure 6. Experimental carbon products turnover frequency (TOF) at different potentials for each M-N-C catalyst using metallic mass determined from ICP-MS (A); TOF normalized by surface metallic composition and BET surface area (B).

In a second set of experiments, stability of the different M-N-C was put to the test at a current density of 100 mA cm^{-2} (Figure 7). The chronopotentiometric experiments ran for 24 hours. Remarkably, without exception all M-N-C showed high stability and no signs of degradation during the measured time. N-C showed however a deactivating profile after 12 hours indicative of the beneficial role of the metallic species in stabilizing N functionalities. The lower amount of active sites in this sample might be responsible for the more negative working potentials that contribute to the degradation of the catalyst. The cathodic potential decreased over time due to the increase in pH and conductivity over time (Figure S18) caused by the hydroxide formation (equation 5 to 7) and potassium ions crossover through the Nafion® membrane, respectively.

$$CO_2 + H_2O + 2e^- \rightarrow CO + 2OH^- \quad (5)$$

$$CO_2 + H_2O + 2e^- \rightarrow HCOO^- + OH^- \quad (6)$$

$$OH^- + CO_2 \rightarrow HCO_3^- \quad (7)$$

The CO selectivity was stable around 90% Faradaic efficiency with Ni-N-C as catalyst. This corresponds to a continuous production of 381 L $m^{-2}h^{-1}$. Sn-N-C achieved an average selectivity towards $HCOO^-$ of 64.2% corresponding to a productivity of 585 g $m^{-2}h^{-1}$. Additionally, Sn-N-C operated at an average of 10.8% selectivity towards CO. Due to the high current densities imposed, the cathode operated at high overpotentials, which suppresses the production of carbon products when using Mn-N-C and Fe-N-C. These, as reported above, showed negligible ERC selectivity at more negative potentials than -1.03 V (Mn-N-C) and -0.83 V (Fe-N-C), due to CO poisoning of the active sites. Co-N-C exhibited the lowest overpotentials at the imposed current and remained stable throughout the 24 hour measurement using around 20 % of the applied current for the production of CO. The high stability and selectivity of Ni-N-C and Sn-N-C point to the conclusion that these are suitable alternatives for scaled up operation. Energy efficiencies of 30.9% for the production of CO and 28.6% for the production of $HCOO^-$ are comparable to reported values using silver and tin nanoparticles [51,52].

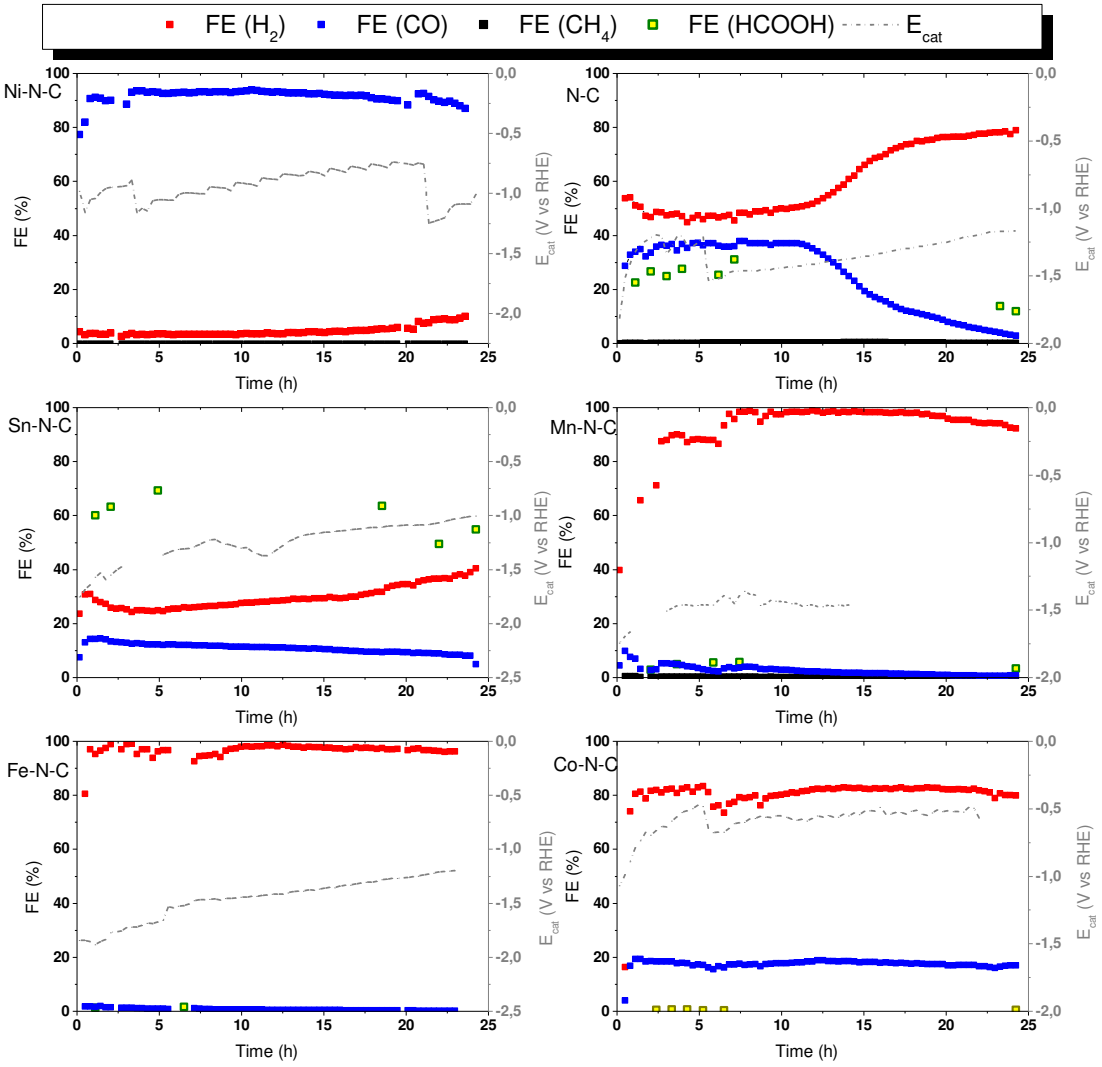

Figure 7. Stability of M-N-C and N-C catalysts operating in chronopotentiometric mode (J=100 mA cm^{-2}).

Finally, we carried out a set of experiments with the best-performing M-N-C catalysts – Ni-N-C and Sn-N-C – at current densities of 200 mA cm^{-2} (Figure 8). These were benchmarked against a GDE coated with 2.0 mg cm^{-2} of silver nanoparticles (<100 nm, Sigma Aldrich). Ni-N-C performs with similar productivity towards CO (711 L $m^{-2}h^{-1}$) when compared to Ag and achieves a reduction of 250 mV in terms of the required overpotential. Sn-N-C is able to reduce CO_2 with 50 to 60% selectivity and requires also significantly lower overpotentials than Ag. Besides, a final figure of merit is the fact that this performance is achieved with only a fraction of the metallic mass (36 µg Ni cm^{-2} and 176 µg Sn cm^{-2} as compared to 2 mg Ag cm^{-2}). This further evidences the potential of this type of catalysts as promising, cheap and abundant alternative for the currently applied noble metal Ag catalysts for the production of CO through electrochemical CO_2 reduction at a large scale.

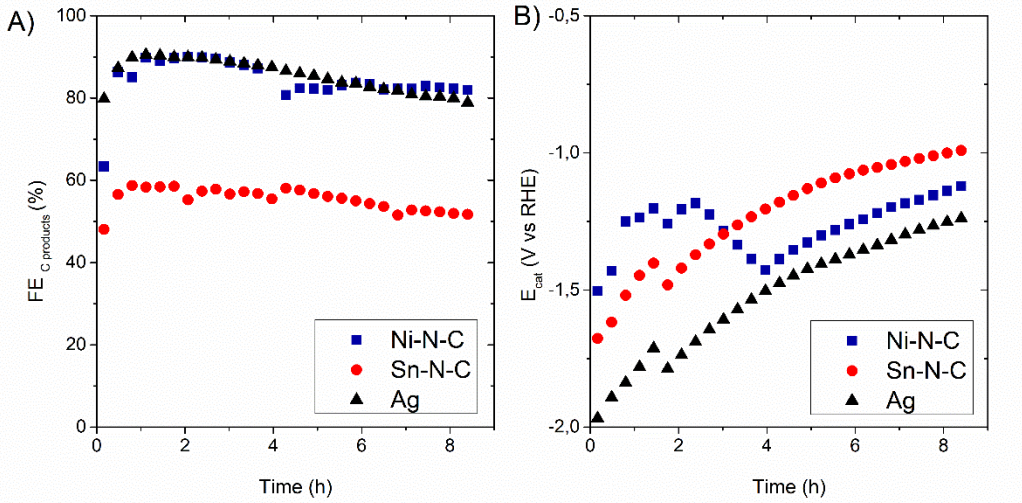

Figure 8. Performance of Ni-N-C, Sn-N-C and Ag catalysts operating at 200 mA cm^{-2}.

In Table 2, the results from our work are depicted alongside other published studies on long-term operation of M-N-C, concerning the Faradaic efficiencies towards CO and $HCOO^-$, the partial current density and the electrolysis time. Due to the high variety of reaction parameters

and the different research goals, a direct comparison of the results is difficult to make. Remarkably, a very limited amount of reports were found regarding the ERC using nitrogen-doped carbon catalysts in combination with flow reactors. In this work an increase of one order of magnitude in the operating current density towards $HCOO^-$ was achieved while maintaining the state-of-the-art stability. The performance of Ni-N-C is comparable to the best-performing reports in literature in terms of selectivity, activity and stability. Furthermore, due to a threefold increase in electrode area compared to the study of *Moller et al*, unprecedented CO productivities were achieved. This summary again highlights the importance of this work as the results achieved here are comparable to and even above the current state-of-the-art, especially in terms of stability at high operating current densities. Further research is still needed to assess the performance of these catalysts at even higher current densities. Novel reactor configurations that allow operation in the absence of catholyte and at lower cell voltages – zero-gap configuration – should be evaluated in order to gauge M-N-C catalysts applicability in comparison with recent reports that use commercial catalysts [53].

Table 2. Overview of literature reports using M-N-C for the production of CO and $HCOO^-$.

Catalyst	**Product**	**Faradaic efficiency (%)**	**Partial current density (mA cm^{-2})**	**Electrolysis time (h)**	**Flow reactor**	**Ref**
Ni-N-C	CO	96	8.2	9	No	[28]
(Cl, N)-Mn/G	CO	97	10	12	No	[31]
Ni–N–AC–B1	CO	70-90	35 - 45	24	Yes	[32]

Ni-N-C	CO	85	170	20	Yes	[33]
$Co_{0.75}Ni_{0.25}$/N-C NFs	CO	85	13.4	20	No	[54]
Fe/Ni-N-C	CO	90	9	50	No	[55]
NiN-GS	CO	90	54	20	Yes	[56]
Bi@NPC	$HCOO^-$	91	12.7	20	No	[57]
Cu(1)Sn(4)-N-CC	$HCOO^-$	84-90	15.6	20	No	[34]
SnO_2@N-CNW	$HCOO^-$	90	11.7	20	No	[58]
Ni-N-C	CO	82	141	0.75	Yes	This work
Ni-N-C	CO	85	170.2	8	Yes	This work
Ni-N-C	CO	95	95	24	Yes	This work
Sn-N-C	$HCOO^-$	68	109	0.75	Yes	This work
Sn-N-C	$HCOO^-$	37	74.4	8	Yes	This work
Sn-N-C	$HCOO^-$	70	70	24	Yes	This work

Conclusions

In summary, we have synthesized and tested a family of nitrogen-doped catalysts with different embedded transition metals (Ni, Co, Sn, Fe and Mn) for the ECR in a continuous flow electrolyzer. The metal species incorporated into the macrocyclic structure proved to have a determining role in the catalytic behavior as well as in the physicochemical properties of the electrode. Co-N-C catalyzed preferentially the HER, while Mn-N-C and Fe-N-C were selective to CO only at mild cathodic potentials. Ni-N-C and Sn-N-C outperformed the alternatives with high activity at moderate and large overpotentials. They achieved an unprecedented productivity of 589 L CO $m^{-2}h^{-1}$ at -1.39 V and 751 g $HCOO^-$ $m^{-2}h^{-1}$ at -1.47 V respectively. All M-N-C remained stable for 24 hours at 100 mA cm^{-2}. The best-performing M-N-C (Ni-N-C and Sn-N-C) were tested at 200 mA cm^{-2} and compared with commercial Ag GDEs. Ni-N-C achieved comparable productivities to commercial Ag GDEs at reduced overpotentials (approx. 250 mV lower). This was accomplished with a remarkable metallic loading between 36 and 176 µg cm^{-2} as compared to the 2 mg cm^{-2} for Ag, underlining the importance of this research. Its facile synthesis method and its earth-abundant components, alongside its outperformance of most literature reports, especially in terms of stability at elevated current density, make these catalysts promising and viable alternatives for the scalability of CO_2 electrolyzers to formate and carbon monoxide.

Associated content

Supporting information

The following files are available free of charge at…

Acknowledgements

The authors acknowledge sponsoring from the research foundation of Flanders (FWO) in the frame of a post-doctoral grant (12Y3919N – ND). This project was co-funded by the Interreg 2 Seas-Program 2014-2020, co-financed by the European Fund for Regional Development in the frame of subsidiary contract nr. 2S03-019. This work was further performed in the framework of the Catalisti MOT project D2M ("Dioxide to Monoxide (D2M): Innovative catalysis for CO_2 to CO conversion"). We thank Lien Pacquets for analyzing the samples with SEM-EDX, Saskia Defossé for helping with the N_2 physisorption measurements and Kitty Baert (VUB) for analyzing the samples with XPS and Raman.

References

[1] C. Hepburn, E. Adlen, J. Beddington, E.A. Carter, S. Fuss, N. Mac Dowell, J.C. Minx, P. Smith, C.K. Williams, The technological and economic prospects for CO2 utilization and removal, Nature. 575 (2019) 87–97. doi:10.1038/s41586-019-1681-6.

[2] P. De Luna, C. Hahn, D. Higgins, S.A. Jaffer, T.F. Jaramillo, E.H. Sargent, What would it take for renewably powered electrosynthesis to displace petrochemical processes?, Science (80-.). 364 (2019). doi:10.1126/science.aav3506.

[3] J.M. Spurgeon, B. Kumar, A comparative technoeconomic analysis of pathways for commercial electrochemical CO2 reduction to liquid products, Energy Environ. Sci. 11

(2018) 1536–1551. doi:10.1039/c8ee00097b.

[4] M. Jouny, W.W. Luc, F. Jiao, A General Techno-Economic Analysis of CO 2 Electrolysis Systems, Ind. Eng. Chem. Res. 57 (2018) 2165–2177. doi:10.1021/acs.iecr.7b03514.

[5] S. Ma, R. Luo, J.I. Gold, A.Z. Yu, P.J.A. Kenis, Carbon nanotube containing Ag catalyst layers for efficient and selective reduction of carbon dioxide †, J. Mater. Chem. A Mater. Energy Sustain. 4 (2016) 8573–8578. doi:10.1039/C6TA00427J.

[6] P.C. Munasinghe, S.K. Khanal, Biomass-derived syngas fermentation into biofuels: Opportunities and challenges, Bioresour. Technol. 101 (2010) 5013–5022. doi:10.1016/j.biortech.2009.12.098.

[7] N.S. Romero Cuellar, K. Wiesner-Fleischer, M. Fleischer, A. Rucki, O. Hinrichsen, Advantages of CO over CO 2 as reactant for electrochemical reduction to ethylene, ethanol and n-propanol on gas diffusion electrodes at high current densities, Electrochim. Acta. 307 (2019) 164–175. doi:10.1016/j.electacta.2019.03.142.

[8] J. Eppinger, K.W. Huang, Formic Acid as a Hydrogen Energy Carrier, ACS Energy Lett. 2 (2017) 188–195. doi:10.1021/acsenergylett.6b00574.

[9] B. Endrődi, E. Kecsenovity, A. Samu, F. Darvas, R. V. Jones, V. Török, A. Danyi, C. Janáky, Multilayer Electrolyzer Stack Converts Carbon Dioxide to Gas Products at High Pressure with High Efficiency, ACS Energy Lett. 4 (2019) 1770–1777. doi:10.1021/acsenergylett.9b01142.

[10] C.T. Dinh, D. Sinton, High Rate, Selective and Stable Electroreduction of CO2 to CO in Basic and Neutral Media, (2018). doi:10.1021/acsenergylett.8b01734.

[11] T. Haas, R. Krause, R. Weber, M. Demler, G. Schmid, Technical photosynthesis involving CO2 electrolysis and fermentation, Nat. Catal. 1 (2018) 32–39. doi:10.1038/s41929-017-

0005-1.

[12] C. Link, A. Wuttig, M. Yaguchi, K. Motobayashi, M. Osawa, Y. Surendranath, Inhibited proton transfer enhances Au-catalyzed CO 2 -to-fuels selectivity, (2018). doi:10.1073/pnas.1602984113.

[13] M. Liu, Y. Pang, B. Zhang, P. De Luna, O. Voznyy, J. Xu, X. Zheng, C.T. Dinh, F. Fan, C. Cao, F.P.G. De Arquer, T.S. Safaei, A. Mepham, A. Klinkova, E. Kumacheva, T. Filleter, D. Sinton, S.O. Kelley, E.H. Sargent, Enhanced electrocatalytic CO2 reduction via field-induced reagent concentration, Nature. 537 (2016) 382–386. doi:10.1038/nature19060.

[14] D. Gao, H. Zhou, J. Wang, S. Miao, F. Yang, G. Wang, J. Wang, X. Bao, Size-Dependent Electrocatalytic Reduction of CO2 over Pd Nanoparticles, J. Am. Chem. Soc. 137 (2015) 4288–4291. doi:10.1021/jacs.5b00046.

[15] K.P. Kuhl, T. Hatsukade, E.R. Cave, D.N. Abram, J. Kibsgaard, T.F. Jaramillo, Electrocatalytic conversion of carbon dioxide to methane and methanol on transition metal surfaces, J. Am. Chem. Soc. 136 (2014) 14107–14113. doi:10.1021/ja505791r.

[16] F. xia Shen, J. Shi, T. you Chen, F. Shi, Q. yuan Li, J. zheng Zhen, Y. fei Li, Y. nian Dai, B. Yang, T. Qu, Electrochemical reduction of CO2 to CO over Zn in propylene carbonate/tetrabutylammonium perchlorate, J. Power Sources. 378 (2018) 555–561. doi:10.1016/j.jpowsour.2017.12.078.

[17] J. Medina-Ramos, J.L. Dimeglio, J. Rosenthal, Efficient reduction of CO2to CO with high current density using in situ or ex situ prepared bi-based materials, J. Am. Chem. Soc. 136 (2014) 8361–8367. doi:10.1021/ja501923g.

[18] M. Asadi, K. Kim, C. Liu, A.V. Addepalli, P. Abbasi, P. Yasaei, P. Phillips, A.

Behranginia, J.M. Cerrato, R. Haasch, P. Zapol, B. Kumar, R.F. Klie, J. Abiade, L.A. Curtiss, A. Salehi-Khojin, Nanostructured transition metal dichalcogenide electrocatalysts for CO2 reduction in ionic liquid, Science (80-.). 353 (2016) 467–470. doi:10.1126/science.aaf4767.

[19] M. Asadi, B. Kumar, A. Behranginia, B.A. Rosen, A. Baskin, N. Repnin, D. Pisasale, P. Phillips, W. Zhu, R. Haasch, R.F. Klie, P. Kra, J. Abiade, A. Salehi-khojin, Robust carbon dioxide reduction on molybdenum disulphide edges, Nat. Commun. (2014) 1–8. doi:10.1038/ncomms5470.

[20] W. Lv, J. Zhou, F. Kong, H. Fang, W. Wang, Porous tin-based film deposited on copper foil for electrochemical reduction of carbon dioxide to formate, Int. J. Hydrogen Energy. 41 (2016) 1585–1591. doi:10.1016/j.ijhydene.2015.11.100.

[21] Anawati, G.S. Frankel, A. Agarwal, N. Sridhar, Degradation and deactivation of Sn catalyst used for CO2 reduction as function of overpotential, Electrochim. Acta. 133 (2014) 188–196. doi:10.1016/j.electacta.2014.04.057.

[22] C. Zhao, J. Wang, J.B. Goodenough, Comparison of electrocatalytic reduction of CO2 to HCOOH with different tin oxides on carbon nanotubes, Electrochem. Commun. 65 (2016) 9–13. doi:10.1016/j.elecom.2016.01.019.

[23] R.L. MacHunda, J. Lee, J. Lee, Microstructural surface changes of electrodeposited Pb on gas diffusion electrode during electroreduction of gas-phase CO2, Surf. Interface Anal. 42 (2010) 564–567. doi:10.1002/sia.3245.

[24] X. Lu, D.Y.C. Leung, H. Wang, J. Xuan, A high performance dual electrolyte microfluidic reactor for the utilization of CO 2, Appl. Energy. 194 (2017) 549–559. doi:10.1016/j.apenergy.2016.05.091.

[25] J. Wu, S. Ma, J. Sun, J.I. Gold, C. Tiwary, B. Kim, L. Zhu, N. Chopra, I.N. Odeh, R. Vajtai, A.Z. Yu, R. Luo, J. Lou, G. Ding, P.J.A. Kenis, P.M. Ajayan, A metal-free electrocatalyst for carbon dioxide reduction to multi-carbon hydrocarbons and oxygenates, Nat. Commun. 7 (2016) 1–6. doi:10.1038/ncomms13869.

[26] X. Liu, L. Dai, Carbon-based metal-free catalysts, Nat. Rev. Mater. 1 (2016). doi:10.1038/natrevmats.2016.64.

[27] G. Wu, K.L. More, C.M. Johnston, P. Zelenay, High-performance electrocatalysts for oxygen reduction derived from polyaniline, iron, and cobalt, Science (80-.). 332 (2011) 443–447. doi:10.1126/science.1200832.

[28] F. Pan, W. Deng, carlos; Justiniano, W. Li, Identification of champion transition metals centers in metal and nitrogen codoped carbon catalysts for CO2 reduction, Appl. Catal. B Environ. 226 (2018) 463–472. doi:10.1016/j.apcatb.2018.01.001.

[29] N. Daems, X. Sheng, I.F.J. Vankelecom, P.P. Pescarmona, Metal-free doped carbon materials as electrocatalysts for the oxygen reduction reaction, J. Mater. Chem. A. 2 (2014) 4085–4110. doi:10.1039/c3ta14043a.

[30] Q. Bi, X. Wang, F. Gu, X. Du, H. Bao, G. Yin, J. Liu, F. Huang, Prominent Electron Penetration through Ultrathin Graphene Layer from FeNi Alloy for Efficient Reduction of CO2 to CO, ChemSusChem. 10 (2017) 3044–3048. doi:10.1002/cssc.201700787.

[31] B. Zhang, J. Zhang, J. Shi, D. Tan, L. Liu, F. Zhang, C. Lu, Z. Su, X. Tan, X. Cheng, B. Han, L. Zheng, J. Zhang, Manganese acting as a high-performance heterogeneous electrocatalyst in carbon dioxide reduction, Nat. Commun. 10 (2019) 1–8. doi:10.1038/s41467-019-10854-1.

[32] N. Daems, B. De Mot, D. Choukroun, K. Van Daele, C. Li, A. Hubin, S. Bals, J.

Hereijgers, T. Breugelmans, Nickel-containing N-doped carbon as effective electrocatalysts for the reduction of CO2 to CO in a continuous-flow electrolyzer, Sustain. Energy Fuels. 4 (2020) 1296–1311. doi:10.1039/c9se00814d.

[33] T. Möller, W. Ju, A. Bagger, X. Wang, F. Luo, T. Ngo Thanh, A.S. Varela, J. Rossmeisl, P. Strasser, Efficient CO 2 to CO electrolysis on solid Ni-N-C catalysts at industrial current densities, Energy Environ. Sci. 12 (2019) 640–647. doi:10.1039/c8ee02662a.

[34] L. Peng, Y. Wang, I. Masood, B. Zhou, Y. Wang, J. Lin, J. Qiao, F.-Y. Zhang, Self-growing Cu/Sn Bimetallic Electrocatalysts on Nitrogen-Doped Porous Carbon Cloth with 3D-Hierarchical Honeycomb Structure for Highly Active Carbon Dioxide Reduction, Appl. Catal. B Environ. (n.d.). doi:10.1016/j.apcatb.2019.118447.

[35] D. Choukroun, N. Daems, T. Kenis, T. Van Everbroeck, J. Hereijgers, T. Altantzis, S. Bals, P. Cool, T. Breugelmans, Bifunctional Nickel-Nitrogen-Doped-Carbon-Supported Copper Electrocatalyst for CO2 Reduction, J. Phys. Chem. C. 124 (2020) 1369–1381. doi:10.1021/acs.jpcc.9b08931.

[36] X. Wang, Z. Wang, F.P.G. De Arquer, C. Dinh, A. Ozden, Y.C. Li, D. Nam, J. Li, Y. Liu, J. Wicks, Z. Chen, M. Chi, B. Chen, Y. Wang, J. Tam, J.Y. Howe, A. Proppe, P. Todorović, F. Li, T. Zhuang, C.M. Gabardo, A.R. Kirmani, C. Mccallum, S. Hung, Y. Lum, M. Luo, Y. Min, A. Xu, C.P.O. Brien, B. Stephen, B. Sun, A.H. Ip, L.J. Richter, S.O. Kelley, D. Sinton, E.H. Sargent, Efficient electrically powered CO2-to-ethanol via suppression of deoxygenation, Nat. Energy. (2020) 478–486. doi:10.1038/s41560-020-0607-8.

[37] M.G. Kibria, J.P. Edwards, C.M. Gabardo, C.T. Dinh, A. Seifitokaldani, D. Sinton, E.H. Sargent, Electrochemical CO2 Reduction into Chemical Feedstocks: From Mechanistic

Electrocatalysis Models to System Design, Adv. Mater. 31 (2019) 1–24. doi:10.1002/adma.201807166.

[38] M. Duarte, B. De Mot, J. Hereijgers, T. Breugelmans, Electrochemical Reduction of CO2: Effect of Convective CO2 Supply in Gas Diffusion Electrodes, ChemElectroChem. 6 (2019) 5596–5602. doi:10.1002/celc.201901454.

[39] TUINSTRA F, KOENIG JL, Raman Spectrum of Graphite, J. Chem. Phys. 53 (1970) 1126–1130. doi:10.1063/1.1674108.

[40] K.T. Lee, X. Ji, M. Rault, L.F. Nazar, Simple synthesis of graphitic ordered mesoporous carbon materials by a solid-state method using metal phthalocyanines, Angew. Chemie - Int. Ed. 48 (2009) 5661–5665. doi:10.1002/anie.200806208.

[41] J. Li, P. Pršlja, T. Shinagawa, A.J. Martín Fernández, F. Krumeich, K. Artyushkova, P. Atanassov, A. Zitolo, Y. Zhou, R. García-Muelas, N. López, J. Pérez-Ramírez, F. Jaouen, Volcano trend in electrocatalytic co2 reduction activity over atomically dispersed metal sites on nitrogen-doped carbon, ACS Catal. 9 (2019) 10426–10439. doi:10.1021/acscatal.9b02594.

[42] D.J. Briggs, Surface Analysis of Polymers by XPS and Static SIMS, Cambridge University Press, 1998.

[43] N. Daems, B. De Mot, D. Choukroun, K. Van Daele, C. Li, A. Hubin, S. Bals, J. Hereijgers, T. Breugelmans, Nickel-containing N-doped carbon as effective electrocatalysts for the reduction of CO 2 to CO in a continuous-flow electrolyzer, Sustain. Energy Fuels. 4 (2020) 1296–1311. doi:10.1039/C9SE00814D.

[44] C. Yan, H. Li, Y. Ye, H. Wu, F. Cai, R. Si, J. Xiao, S. Miao, S. Xie, F. Yang, Y. Li, G. Wang, X. Bao, Coordinatively unsaturated nickel-nitrogen sites towards selective and

high-rate CO2 electroreduction, Energy Environ. Sci. 11 (2018) 1204–1210. doi:10.1039/c8ee00133b.

[45] S. Ren, D. Joulié, D. Salvatore, K. Torbensen, M. Wang, M. Robert, C.P. Berlinguette, Molecular electrocatalysts can mediate fast, selective CO2 reduction in a flow cell, Science (80-.). 365 (2019) 367–369. doi:10.1126/science.aax4608.

[46] F. Franco, C. Rettenmaier, H.S. Jeon, B. Roldan Cuenya, Transition metal-based catalysts for the electrochemical CO_2 reduction: from atoms and molecules to nanostructured materials, Chem. Soc. Rev. (2020). doi:10.1039/D0CS00835D.

[47] J. Schneider, H. Jia, J.T. Muckerman, E. Fujita, Thermodynamics and kinetics of CO2, CO, and H+ binding to the metal centre of CO2 reduction catalysts, Chem. Soc. Rev. 41 (2012) 2036–2051. doi:10.1039/c1cs15278e.

[48] Z. Geng, Y. Cao, W. Chen, X. Kong, Y. Liu, T. Yao, Y. Lin, Regulating the coordination environment of Co single atoms for achieving efficient electrocatalytic activity in CO2 reduction, Appl. Catal. B Environ. 240 (2019) 234–240. doi:10.1016/j.apcatb.2018.08.075.

[49] T.N. Huan, N. Ranjbar, G. Rousse, M. Sougrati, A. Zitolo, V. Mougel, F. Jaouen, M. Fontecave, Electrochemical Reduction of CO2 Catalyzed by Fe-N-C Materials: A Structure-Selectivity Study, ACS Catal. 7 (2017) 1520–1525. doi:10.1021/acscatal.6b03353.

[50] W. Ju, A. Bagger, G.P. Hao, A.S. Varela, I. Sinev, V. Bon, B. Roldan Cuenya, S. Kaskel, J. Rossmeisl, P. Strasser, Understanding activity and selectivity of metal-nitrogen-doped carbon catalysts for electrochemical reduction of CO2, Nat. Commun. 8 (2017) 1–9. doi:10.1038/s41467-017-01035-z.

[51] T. Haas, R. Krause, R. Weber, M. Demler, G. Schmid, Technical photosynthesis involving CO2electrolysis and fermentation, Nat. Catal. 1 (2018) 32–39. doi:10.1038/s41929-017-0005-1.

[52] H. Jiang, Y. Zhao, L. Wang, Y. Kong, F. Li, P. Li, Electrochemical CO2 reduction to formate on Tin cathode: Influence of anode materials, J. CO2 Util. 26 (2018) 408–414. doi:10.1016/j.jcou.2018.05.029.

[53] B. Endrődi, E. Kecsenovity, A. Samu, T. Halmágyi, S. Rojas-Carbonell, L. Wang, Y. Yan, C. Janáky, High carbonate ion conductance of a robust PiperION membrane allows industrial current density and conversion in a zero-gap carbon dioxide electrolyzer cell, Energy Environ. Sci. (2020) 4098–4105. doi:10.1039/d0ee02589e.

[54] W. Zhang, J. Zeng, H. Liu, Z. Shi, Y. Tang, Q. Gao, CoxNi1−x nanoalloys on N-doped carbon nanofibers: Electronic regulation toward efficient electrochemical CO2 reduction, J. Catal. 372 (2019) 277–286. doi:10.1016/j.jcat.2019.03.014.

[55] P. Lu, J. Zhang, H. He, M. Wang, Z. Luo, D. Gao, Iron / nickel nano-alloy encapsulated in nitrogen-doped carbon framework for CO 2 electrochemical conversion with prominent CO selectivity, (2019). doi:10.1016/j.jpowsour.2019.227496.

[56] K. Jiang, S. Siahrostami, A.J. Akey, Y. Li, Z. Lu, J. Lattimer, Y. Hu, C. Stokes, M. Gangishetty, G. Chen, Y. Zhou, W. Hill, W. Bin Cai, D. Bell, K. Chan, J.K. Nørskov, Y. Cui, H. Wang, Transition-Metal Single Atoms in a Graphene Shell as Active Centers for Highly Efficient Artificial Photosynthesis, Chem. 3 (2017) 950–960. doi:10.1016/j.chempr.2017.09.014.

[57] D. Zhang, Z. Tao, F. Feng, B. He, W. Zhou, J. Sun, J. Xu, Q. Wang, L. Zhao, Electrochimica Acta High ef fi ciency and selectivity from synergy : Bi nanoparticles

embedded in nitrogen doped porous carbon for electrochemical reduction of CO 2 to formate, Electrochim. Acta. 334 (2020) 135563. doi:10.1016/j.electacta.2019.135563.

[58] B. Zhang, L. Sun, Y. Wang, S. Chen, J. Zhang, Well-dispersed SnO2 nanocrystals on N-doped carbon nanowires as efficient electrocatalysts for carbon dioxide reduction, J. Energy Chem. 41 (2020) 7–14. doi:10.1016/j.jechem.2019.04.022.